REPORT

SOLAR CELLS

Impact of strain relaxation on performance of α-formamidinium lead iodide perovskite solar cells

Gwisu Kim*, Hanul Min*, Kyoung Su Lee, Do Yoon Lee, So Me Yoon, Sang Il Seok†

High-efficiency lead halide perovskite solar cells (PSCs) have been fabricated with α-phase formamidinium lead iodide ($FAPbI_3$) stabilized with multiple cations. The alloyed cations greatly affect the bandgap, carrier dynamics, and stability, as well as lattice strain that creates unwanted carrier trap sites. We substituted cesium (Cs) and methylenediammonium (MDA) cations in FA sites of $FAPbI_3$ and found that 0.03 mol fraction of both MDA and Cs cations lowered lattice strain, which increased carrier lifetime and reduced Urbach energy and defect concentration. The best-performing PSC exhibited power conversion efficiency >25% under 100 milliwatt per square centimeter AM 1.5G illumination (24.4% certified efficiency). Unencapsulated devices maintained >80% of their initial efficiency after 1300 hours in the dark at 85°C.

The lead halide perovskite structure is represented by the general chemical formula $APbX_3$, where A denotes an organic ammonium or inorganic cation such as methylammonium (MA^+), formamidinium (FA^+), or Cs^+; and X denotes a halide (I^-, Br^-, or Cl^-). Corner-shared PbX_6 octahedra form a cuboctahedral cage to accommodate the A cation that satisfies the steric requirements and stabilize three-dimensional perovskite structure. The optoelectrical properties of $APbX_3$ perovskites are dominated by the inorganic lead halide lattice, while the cation in the A site contributes to the stabilization of the structure (*1*). Therefore, the bandgap of the perovskite depends primarily on halides and is relatively less affected by the A cation. Thus, the factors affecting device performance, such as dielectric properties (*2*) and distortion (*3*), can be easily controlled by the proper selection or combination of A cations without compromising the bandgap.

Although MA^+, FA^+, and Cs^+ are the most well studied A cations for the $APbI_3$ perovskite with the narrowest bandgap capable of absorbing a wide range of sunlight (*4*–*7*), it is difficult to use $APbI_3$ with FA^+ and Cs^+ cations in a solar cell because it is thermodynamically unstable at room temperature and crystallizes into the δ-phase (a very wide bandgap nonperovskite) from the α-phase (*6*, *8*, *9*). Although the structural stabilization of lead halide perovskite with various cations was explained by the Goldschmidt tolerance (*t*) factor [$t = r_A + r_I = \sqrt{2}(r_{Pb} + r_I)$, where r_A, r_{Pb}, and r_I are the radii of the A cation, Pb cation, and I anion, respectively] (*1*, *10*), it can be achieved by distorting PbI_6 octahedron or by N–H···I hydrogen bonding with organic cations (*1*). Currently, high-efficiency perovskite solar cells (PSCs) are predominately fabricated with $FAPbI_3$, for which phase stabilization is achieved by controlling *t* through the synergistic entropic effect of mixing MA^+, Cs^+, and Br^- (*5*, *11*–*14*). However, as the composition of $FAPbI_3$ is changed to stabilize the perovskite structure of the α-phase, the bandgap may widen. Moreover, the local strain can increase because of the distortion of the ideal structure, including tilting, deformation, expansion, and shrinkage of the octahedral network (*15*–*17*).

The residual strain in halide perovskites substantially affects the performance of PSCs by reducing structural stability (*18*, *19*), decreasing the carrier mobility (*20*), and suppressing atomic vacancies (*21*). Lattice strain was directly related to increased defect concentration and nonradiative recombination, which is associated with the efficiency (*22*). Huang and colleagues reported the reduction of residual strain by thermal annealing of perovskite films produced by a solution process enhanced the intrinsic stability of the films under illumination by decreasing ion migration (*23*). Chen and colleagues (*24*) demonstrated that α-$FAPbI_3$ can be stabilized by growing a single crystal on the substrate and that the bandgap and hole mobility changed when a compressive strain was applied.

Alloyed mixed-halide perovskites are nonuniform because of the phase separation through segregation of ions, which causes local lattice mismatch and leads to residual deformation. The efficiency was increased by improving carrier transport and extraction at the interface of the perovskite absorber and hole transport material (HTM) by controlling the vertically strained gradient with flipped annealing method (*24*). Xue *et al.* (*25*) observed that the stability considerably improved with added compressive strain by using an HTM with a high coefficient of thermal expansion for the perovskite film. Tsai *et al.* (*26*) reported improved PSC device performance under continuous light illumination owing to the uniform lattice expansion in the perovskite film.

The strain in $APbI_3$ perovskite can also be reduced by substituting some of the Pb^{2+} ions with isovalent Cd^{2+} ions of a small ionic radius (*21*, *27*). As a result, both the efficiency and stability improved with the relaxation of the local lattice strain. Similarly, it was shown for mixed $(FASnI_3)_{0.5}(MAPbI_3)_{0.5}$ PSCs that the addition of 2.5 mol % of Cs^+ ions led to the relaxation of the lattice strain, resulting in a lower concentration of defects, which in turn improved efficiency (*28*). Therefore, the strain engineering of lead halide perovskites has attracted attention as a method to further improve both the efficiency and stability of PSCs.

Recently, we reported the stabilization of α-$FAPbI_3$ by substituting FA^+ with the slightly larger methylenediammonium (MDA^{2+}) (*29*). Compared with stabilizing α-phase by adding MA^+ or Cs^+ (both of which have a smaller ionic radius than FA^+), the change in the bandgap resulting from MDA^{2+} substitution is very small (~0.01 eV), and a high short-circuit current (J_{sc}) was obtained with relatively better stability (retaining >90% of initial performance over 600 hours of irradiation). Nevertheless, substituting only MDA^{2+} cations with a larger ionic radius, or Cs^+ with a smaller ionic radius, than FA^+ can distort Pb–I–Pb bonds by tilting the PbI_6 octahedron. One of the most common strain-compensation strategies is to introduce larger and smaller ions together to reduce the local tensile and compressive strain in the perovskite lattice.

In this study, we used the dual substitution of FA^+ sites with MDA^{2+} and Cs^+ in the same molar ratio to relax the lattice strain of MDA-stabilized α-$FAPbI_3$. The alloyed $FAPbI_3$ with 0.03 mol fraction of both MDA and Cs cations effectively reduced the lattice strain and the trap density in the PSCs, resulting in the fabrication of PSCs with 24.4 and 21.6% certified efficiency for small and large (1 cm by 1 cm) cells, respectively, through the suppression of nonradiative carrier recombination. Moreover, the corresponding devices exhibited superior thermal stability and maintained >80% of their initial efficiency after 1300 hours in storage at 85°C (at 15 to 25% relative humidity).

The $(FAPbI_3)_{1-x}(MC)_x$ perovskite thin films (with x = 0.01, 0.02, 0.03, or 0.04 mol fraction) were deposited by our solvent engineering process (*29*, *30*) using precursor solutions that dissolved the FAI and PbI_2 with the desired number of MDA^{2+} and Cs^+ cations. Here, MC is an abbreviation that means that MDA^{2+} and Cs^+ were mixed in equimolar amounts (i.e., MDA:Cs = 1:1). Figure 1A shows the x-ray diffraction (XRD) patterns of the samples with different x values for the perovskite thin layers prepared directly on a mesoporous-TiO_2 (mp-TiO_2) electron-transporting layer. In the XRD

Department of Energy Engineering, School of Energy and Chemical Engineering, Ulsan National Institute of Science and Technology, 50 UNIST-gil, Eonyang-eup, Ulju-gun, Ulsan 44919, Korea.
*These authors contributed equally to this work.
†Corresponding author. Email: seoksi@unist.ac.kr

patterns, two dominant peaks could be seen at about 14° and 28°, which we assigned to the characteristic (001) and (002) crystal planes of the α-$FAPbI_3$ phase, and no δ-phase appeared at 11.6°.

As x increased in $(FAPbI_3)_{1-x}(MC)_x$, the diffraction intensity of the two peaks also increased, and no new peaks appeared, which was likely caused by preferred orientation during crystallization on the substrate from the comparison with XRD patterns of powders scraped from the films (fig. S2A). The average crystalline sizes and full width at half maximum of the diffraction peak at the (100) plane did not show a large variation with x and became smaller and broader with the shift of the diffraction angle to the low angle in powder case, owing to residual stress present in the films (fig. S2, B and C). Because crystallographic data measured from one-dimensional XRD typically only provide limited structural information, particularly for highly oriented perovskite films, we obtained two-dimensional grazing-incidence wide-angle x-ray scattering (GIWAXS) patterns to probe changes in the crystallographic orientations of the perovskite film as x was varied.

Distinct and relatively strong spots were observed in the ring patterns (fig. S1A) as x increased (i.e., increased substitution) in $(FAPbI_3)_{1-x}(MC)_x$. The GIWAXS pattern for $x = 0.04$ (Fig. 1B) exhibited a strong diffraction intensity and was similar to that of $x = 0.03$ (fig. S1C) but had slightly greater intensity and appeared more clearly as a mixture of scattered secondary spots and rings. The preferential crystal orientations for α-$FAPbI_3$ were observed out of the plane in the direction $[100]_c$ and $[200]_c$ (Fig. 1B, white arrows). We concluded that the diffraction intensity increased with increasing x because of the highly oriented crystal domains, not the improvements in crystallinity.

In addition, compared with $(FAPbI_3)_{0.972}(MDACl_2)_{0.038}$ (denoted as control), the peak position at ~14° gradually shifted to higher angles from 14.07° to 14.16° as x increased to 0.03, then it slightly decreased to 14.12° at $x = 0.04$ (Fig. 1C). In the same crystal, because the diffraction angle (2θ) reflected the expansion and contraction of the lattice, the diffraction angle could shift depending on the proportion of the relatively smaller Cs^+ and larger MDA^{2+} cations to the FA^+ cations. This result suggested that the incorporation of Cs^+ and MDA^{2+} into the lattice of $FAPbI_3$ formed a solid-state alloy. As shown in fig. S3, this shift in diffraction angle was most consistent with the change in the radius of cations calculated using the ionic radii of individual FA^+, Cs^+, and MDA^{2+}, except at $x = 0.04$ and when considering the FA^+ vacancies for the charge balance without also considering the insertion of Cl^- ions that may result from the bivalent MDA (*29*).

Inferring the deviation from this trend at $x = 0.04$, we expected the composition of the actual perovskite thin film to differ slightly from the composition of the precursor solution. Nevertheless, the change in optical properties with x was negligible. In Fig. 1D, the ultraviolet-visible (UV-vis) absorption spectra and normalized photoluminescence (PL) data with different x mole fraction in $(FAPbI_3)_{1-x}(MC)_x$ and control are compared. A slight blue-shift was

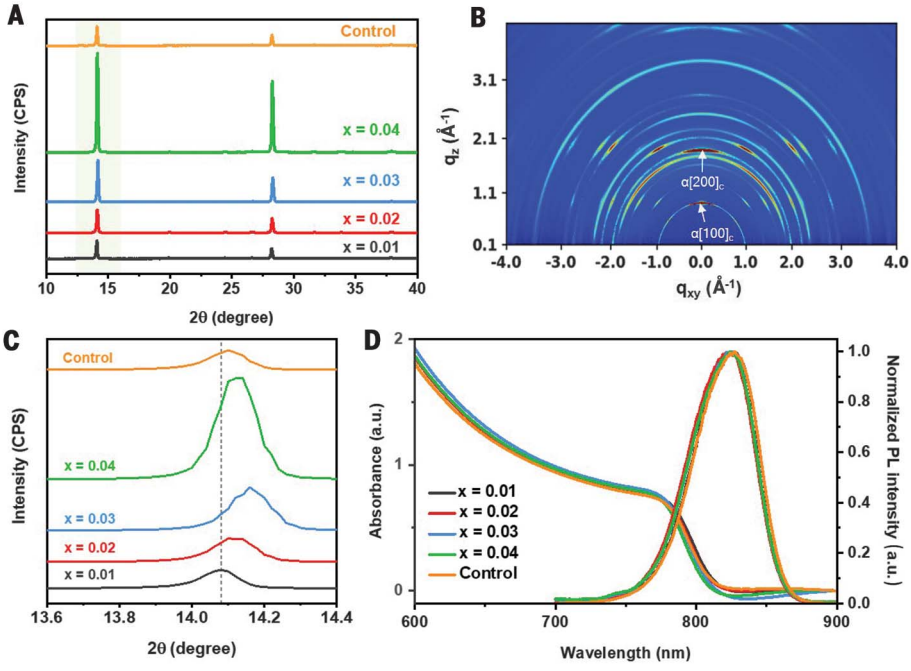

Fig. 1. Characterization of perovskite thin films deposited on mp-TiO_2 for the $(FAPbI_3)_{1-x}(MC)_x$ and control perovskite films. (**A**) XRD patterns of perovskite film. CPS, counts per second. (**B**) GIWAXS pattern for $x = 0.04$. (**C**) Magnified (100) plane diffraction peaks in the region shaded in green in (A). (**D**) UV-vis absorption and normalized PL spectra. a.u., arbitrary units.

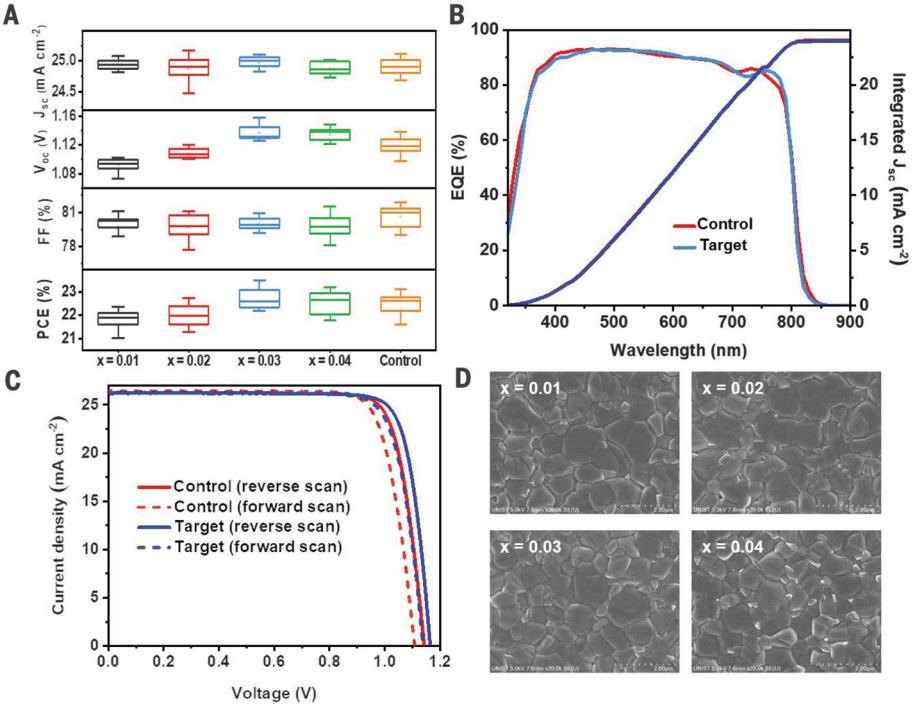

Fig. 2. Performance and surface morphologies of PSCs fabricated with x in $(FAPbI_3)_{1-x}(MC)_x$ and control perovskite films. (**A**) J_{sc}, V_{oc}, FF, and PCE statistics of 24 PSCs. (**B**) EQE curves of target and control PSCs. (**C**) *J-V* curves of target and control PSCs. (**D**) Surface SEM images of perovskite thin layers.

observed in the absorption onset as x increased, however, the shift was very small compared with the composition in which a single Cs^+ cation was added to pure $FAPbI_3$ (*11*). The corresponding shifts are consistent with the PL emission peaks at 826, 825, 825, and 824 nm for x = 0.01, 0.02, 0.03, and 0.04, respectively, and the peak at 827 mm for the control.

Figure 2A shows the variation in solar cell characteristics with different x in $(FAPbI_3)_{1-x}(MC)_x$ and control. The devices comprised multiple layers: glass/fluorine-doped tin oxide (FTO)/compact-TiO_2/thin mp-TiO_2/perovskite/2,2',7,7'-tetrakis[*N*,*N*-di(4-methoxyphenyl)amino]-9,9'-spirobifluorene (Spiro-OMeTAD)/Au. To confirm the effect of cosubstitution of MDA^{2+} and Cs^+ on solar cell performance, at least 24 devices in each category were fabricated and evaluated in one experiment (Fig. 2A). The statistical distribution of factors such as J_{sc}, open-circuit voltage (V_{oc}), and fill factor (FF) determining power conversion efficiency (PCE) showed that a relatively better performance was noticed for x = 0.03 (denoted as target) with a narrow distribution of J_{sc}, V_{oc}, FF, and PCE and an average PCE of 22.72 ± 0.45%.

In general, when the composition or coating process of the perovskite thin film is changed, the surface morphology may change and in turn change the efficiency. Thus, we imaged the surface morphology in $(FAPbI_3)_{1-x}(MC)_x$ and the control films using top-view scanning electron microscopy (SEM) (Fig. 2D). Regardless of the amounts of additives, all films showed a similar grain size without apparent pinholes on the surface. These results indicate that the incorporation with small amounts of Cs^+ and MDA^{2+} cations did not affect the morphological features of the perovskite layers, such as grain sizes and surface roughness.

For simplicity, the control and target were compared to find out why the efficiency improved by substituting the same amount of Cs^+ and MDA^{2+} in $FAPbI_3$. Figure 2B shows the external quantum efficiency (EQE) spectra for one of the representative control and target devices. The EQE onset of the target is slightly blue-shifted, which was consistent with the tuned bandgap (Fig. 1D). Nevertheless, as can be seen in the integrated J_{sc} (Fig. 2B), this small blue shift in the bandgap was not appreciable. The cross-sectional thickness of the control and target devices were compared by using SEM images (fig. S4). There was no noticeable difference in the thicknesses between two representative layers (415 nm for the control and 425 nm for the target). The similarities in J_{sc} implied that there was no substantial difference in the charge collection in the two comparison groups.

The current density-voltage (*J-V*) characteristics of the best-performing control and target devices in a reverse and forward bias sweep with antireflective coatings (fig. S5) on the device surface are compared in Fig. 2C. The J_{sc}, V_{oc}, and FF values calculated from the *J-V* curve of the target were 26.23 mA cm^{-2}, 1.168 V, and 82.15%, respectively; these factors correspond to a PCE of 25.17% under standard air mass (AM) 1.5 conditions, whereas the control exhibited a PCE of 24.48% with J_{sc} = 26.25 mA cm^{-2}, V_{oc} = 1.138 V, and FF = 81.95%. The PCE of the target devices shown in Fig. 2C was certified by an accredited laboratory (Newport, USA) using a quasi-steady-state (QSS) method. The stabilized PCE measured by QSS was 24.37% with J_{sc} = 26.17 mA cm^{-2}, V_{oc} = 1.162 V, and FF = 80.13% for the small cell (fig. S6), and 21.63% for the large cell (1 cm by 1 cm) (fig. S7). Within the scope of this study, the effect of compositional changes on J_{sc} was very limited, and most efficiency improvements were attributable to an increase in V_{oc}. As noted earlier, because control and target devices have almost the same bandgap, surface morphology, and thickness, the large increase in V_{oc} (low V_{oc} loss) arose from the changes inside the crystalline perovskites. The V_{oc} loss for x and control occurred at x = 0.03 (fig. S8).

Generally, V_{oc} loss is directly related to reduction in defect concentration and nonradiative losses (*31*–*34*). In this regard, there have been many reports that lattice strain in perovskites increases defect concentrations and nonradiative recombination (*22*, *24*, *28*, *35*). We estimated the variation in lattice strain of perovskite films with x in $(FAPbI_3)_{1-x}(MC)_x$ using the Williamson–Hall (WH) plot (individual plots with x are displayed in fig. S9)

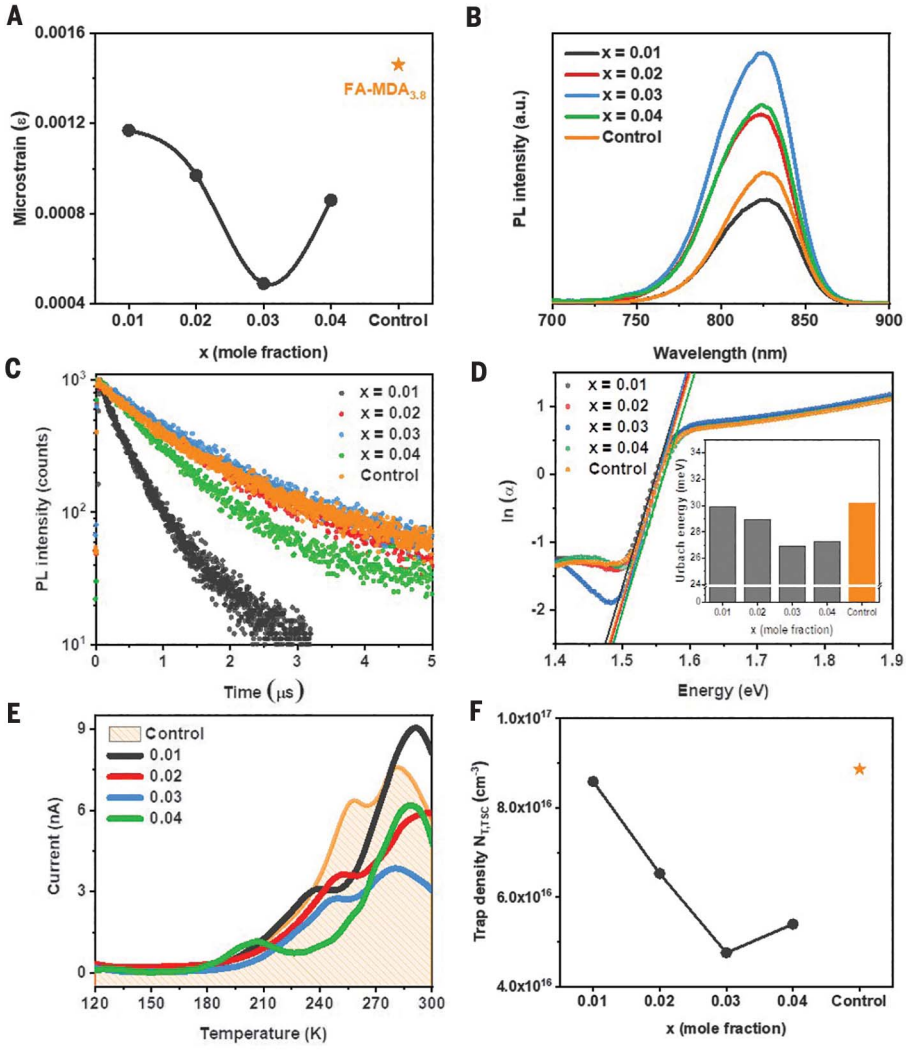

Fig. 3. Defect analysis of perovskite films deposited with x in $(FAPbI_3)_{1-x}(MC)_x$ and control. (**A**) Residual strain calculated in perovskites consisting of FTO/mp-TiO_2/perovskite. (**B**) Steady-state photoluminescence and (**C**) time-resolved photoluminescence spectra of films deposited on glass. (**D**) Logarithm of absorption coefficient (α) versus photon energy and (inset) Urbach energy calculated in perovskites consisting of FTO/mp-TiO_2/perovskite. (**E**) Thermally stimulated current spectra. (**F**) Trap density. The orange star in (A) and (F) indicates control perovskite.

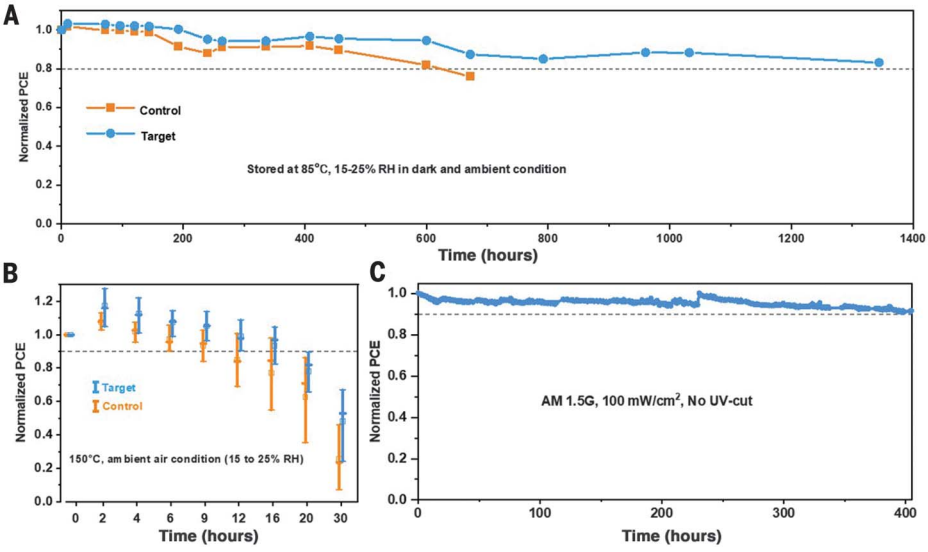

Fig. 4. Long-term stability tests. Comparison of the thermal stability at (**A**) 85°C and (**B**) 150°C of unencapsulated control and target PCSs. (**C**) Maximum power point tracking measured with the encapsulated target device under full solar illumination (AM 1.5G, 100 mW/cm^2 in ambient condition at 25° to 35°C) without a UV filter.

from the XRD patterns of Fig. 1A. As can be seen in Fig. 3A, the strain decreased as x increased from 0.01 to 0.03 and then increased again at 0.04. Here, the WH method considers the broadening of the peak as a function of the diffraction angle, which is assumed to be the combined effect of broadening induced by both the crystalline size and strain (*36*, *37*). Furthermore, the strain of perovskite films can also be attributed from the preferred crystalline phase and oriented domain boundaries, etc. However, the change in crystallite size was not very large (fig. S2), and the variation of strain obtained from the XRD patterns of powders scraped from the thin films was almost similar to that of the films (fig. S10). In particular, when the mole fraction of MDA and Cs incorporated in $FAPbI_3$ was 3:3, the lowest strain appeared. This result proposes that 3:3 substitution of Cs^+ and MDA^{2+} in $FAPbI_3$ effectively mitigated the lattice strain in the perovskite structure (fig. S11). Thus, reducing the strain of the lattice minimized defect centers or traps that can capture charge carriers and negatively affect solar cell performance.

Steady-state PL and time-resolved photoluminescence (TRPL) measurements were carried out to investigate the nonradiative carrier recombination of the perovskite thin films with different x [$(FAPbI_3)_{1-x}(MC)_x$] and control. Figure 3B shows PL spectra for the thin perovskite layers deposited on glass substrate. The addition of equal amounts of Cs^+ and MDA^{2+} increased the PL intensity; the intensity maximized at x = 0.03 and then decreased again at x = 0.04. Under the same conditions, an increase in PL intensity implied a decrease in nonradioactive recombination. For a more quantitative comparison of charge recombination, TRPL was measured using time-correlated single photon counting (TCSPC) under low-intensity pulsed excitation, for which decay dynamics mostly reflect nonradiative trap-assisted recombination. From the PL decay curves in Fig. 3C, the carrier lifetime values were obtained by using the biexponential equation $Y = A_1\exp(-t/\tau_1) + A_2\exp(-t/\tau_2)$, where τ_1 and τ_2 denote the fast and slow decay time and are related to the trap-assisted nonradiative and radiative recombination processes, respectively. As seen in the average carrier lifetime (table S1) measured using six different samples, both τ_1 and τ_2 at x = 0.03 are the longest and longer than control. This increased lifetime was consistent with the reduction of lattice strain, indicating that the relaxation of the strain suppressed nonradiative recombination by reducing the number of trap states.

Changes in the lattice strain can also affect the Urbach energy (E_u). A lower E_u of the perovskite film indicates a higher structural quality of the film, as well as a lower voltage loss between V_{oc} and the bandgap voltage. Figure 3D shows E_u for the perovskite films calculated from UV-vis absorption spectra using the equation $\alpha = \alpha_0 \exp(h\nu/E_u)$, where α is absorption coefficient and $h\nu$ is photon energy. The E_u of the control and target films were 30.18 and 26.88 meV, respectively (Fig. 3D and fig. S12). Interestingly, the change in E_u of $(FAPbI_3)_{1-x}(MC)_x$ perovskite films shows a similar trend with the change in the microstrain of the films. This result implies that the lattice strain is closely related to the trap states in the perovskite films.

To further understand the total quantity and energetic levels of the trap states, thermally stimulated current (TSC) analysis was performed in complete devices. Figure 3E presents the TSC spectra for temperatures from 120 to 300 K for $(FAPbI_3)_{1-x}(MC)_x$–based PSCs compared with the control device. The TSC signal could be integrated to estimate the lower limit of trap densities over the elapsed time according to the equation

$$\int_{\text{signal}} I_{TSC}\,dt \le eN_{T,TSC}Vol$$

where $N_{T,TSC}$ is the trap density, e is the elementary charge, and Vol is the volume of the perovskite layer (*38*, *39*). The trap density of the control device (8.86×10^{16} cm^{-3}) was the highest, which indicates that the strain in the perovskite structure induced an increase in defects. The trap density decreased in the $(FAPbI_3)_{1-x}(MC)_x$ devices from x = 0.01 to x = 0.03, where it was smallest (4.76×10^{16} cm^{-3}), and then increased at x = 0.04 (Fig. 3F).

To extract the activation energy of the trap states, the slope of the initial rise of the TSC current, which was attributed to the start of trap release, in the Arrhenius plot for each condition was fitted to the following equation

$$I_{TSC} \propto \exp\left(-\frac{E_A}{k_B T}\right)$$

where E_A, k_B, and T are the activation energy, Boltzmann constant, and temperature, respectively (*40*, *41*). For the control device, trap states with an activation energy E_{A1} = 150 meV were estimated (fig. S13). For x = 0.01, a higher activation energy (224 meV) was observed, but it was drastically reduced at x = 0.02 (131 meV) and x = 0.03 (130 meV) and then rapidly increased to 272 meV at x = 0.04. A higher activation energy indicates traps formed deeper in the bandgap, which promotes nonradiative recombination. At very low temperatures (<250 K), the activation energy E_{A2} of x = 0.03 (169 meV) was slightly lower than that of the control (183 meV); however, it is speculated that the E_{A1} value is more critical to real operational conditions, which are higher than

room temperature (298 K). The defect analysis, PL, TCSPC, Urbach energy, and TSC results were in good agreement with the changes in the lattice strain of the $(FAPbI_3)_{1-x}(MC)_x$ perovskites, which implies that the enhanced device performance with improved V_{oc} was closely related to defect passivation induced by the strain relaxation of the perovskite structure.

Long-term stability is also very important, even if the efficiency of PSCs is improved by reducing strain. The thermal stability of PSCs with thermally stable poly(triarylamine) as the HTM were compared to rule out thermal degradation from the HTM layer for the control and target devices. Unencapsulated devices were stored at 85°C in an oven under 15 to 25% relative humidity under dark and ambient conditions. The control device retained at least 80% of its initial efficiency up to 600 hours. In contrast, the target device maintained >80% of its initial efficiency even after 1300 hours (Fig. 4A). In addition, control and target devices using copper phthalocyanine as HTM were tested at 150°C without any encapsulation. The target device retained almost 80% of initial PCE after 20 hours, unlike the control device, for which PCE decreased to ~60% of its initial value (Fig. 4B). This improved thermal stability by Cs^+ incorporation is consistent with the reported results (*4*, *5*, *42*–*44*). The long-term operational stability of an encapsulated device (using Spiro-OMeTAD as HTM) was also tested with maximum power point tracking under ambient air and full solar illumination without an ultraviolet cut-off filter (Fig. 4C). The target device maintained >90% of its initial efficiency after 400 hours, which is comparable with other efficient mp-TiO_2–based PSCs (*29*, *45*, *46*).

REFERENCES AND NOTES

1. F. Brivio, A. B. Walker, A. Walsh, *APL Mater.* **1**, 042111 (2013).
2. E. J. Juarez-Perez *et al.*, *J. Phys. Chem. Lett.* **5**, 2390–2394 (2014).
3. D. Ghosh, A. R. Smith, A. B. Walker, M. S. Islam, *Chem. Mater.* **30**, 5194–5204 (2018).
4. D. P. McMeekin *et al.*, *Science* **351**, 151–155 (2016).
5. M. Saliba *et al.*, *Energy Environ. Sci.* **9**, 1989–1997 (2016).
6. N. Pellet *et al.*, *Angew. Chem. Int. Ed.* **53**, 3151–3157 (2014).
7. J.-W. Lee *et al.*, *Adv. Energy Mater.* **5**, 1501310 (2015).
8. Q. Han *et al.*, *Adv. Mater.* **28**, 2253–2258 (2016).
9. C. C. Stoumpos, C. D. Malliakas, M. G. Kanatzidis, *Inorg. Chem.* **52**, 9019–9038 (2013).
10. V. M. Goldschmidt, *Naturwissenschaften* **14**, 477–485 (1926).
11. C. Yi *et al.*, *Energy Environ. Sci.* **9**, 656–662 (2016).
12. M. Saliba *et al.*, *Science* **354**, 206–209 (2016).
13. Z. Wang *et al.*, *Nat. Energy* **2**, 17135 (2017).
14. D. Luo *et al.*, *Science* **360**, 1442–1446 (2018).
15. C. Grote, R. F. Berger, *J. Phys. Chem. C* **119**, 22832–22837 (2015).
16. N. Rolston *et al.*, *Adv. Energy Mater.* **8**, 1802139 (2018).
17. L. Zhang *et al.*, *Sci. Rep.* **8**, 7760 (2018).
18. X. Zheng *et al.*, *ACS Energy Lett.* **1**, 1014–1020 (2016).
19. Y. Chen *et al.*, *Nature* **577**, 209–215 (2020).
20. K. Nishimura *et al.*, *ACS Appl. Mater. Interfaces* **11**, 31105–31110 (2019).
21. M. I. Saidaminov *et al.*, *Nat. Energy* **3**, 648–654 (2018).
22. T. W. Jones *et al.*, *Energy Environ. Sci.* **12**, 596–606 (2019).
23. J. Zhao *et al.*, *Sci. Adv.* **3**, eaao5616 (2017).
24. C. Zhu *et al.*, *Nat. Commun.* **10**, 815 (2019).
25. D.-J. Xue *et al.*, *Nat. Commun.* **11**, 1514 (2020).
26. H. Tsai *et al.*, *Science* **360**, 67–70 (2018).
27. H. Wang *et al.*, *Adv. Mater.* **31**, e1904408 (2019).
28. G. Kapil *et al.*, *ACS Energy Lett.* **4**, 1991–1998 (2019).
29. H. Min *et al.*, *Science* **366**, 749–753 (2019).
30. N. J. Jeon *et al.*, *Nat. Mater.* **13**, 897–903 (2014).
31. T. Leijtens *et al.*, *Energy Environ. Sci.* **9**, 3472–3481 (2016).
32. X. Zheng *et al.*, *Nat. Energy* **2**, 17102 (2017).
33. J.-F. Liao *et al.*, *J. Mater. Chem. A Mater. Energy Sustain.* **7**, 9025–9033 (2019).
34. J. J. Yoo *et al.*, *Energy Environ. Sci.* **12**, 2192–2199 (2019).
35. J. T.-W. Wang *et al.*, *Energy Environ. Sci.* **9**, 2892–2901 (2016).
36. G. K. Williamson, W. H. Hall, *Acta Metall.* **1**, 22–31 (1953).
37. B. D. Cullity, S. R. Stock, *Elements of X-Ray Diffraction* (Prentice-Hall, ed. 3, 2001).
38. G. Gordillo, C. A. Otálora, M. A. Reinoso, *J. Appl. Phys.* **122**, 075304 (2017).
39. Y. Hu *et al.*, *Adv. Energy Mater.* **8**, 1703057 (2018).
40. G. F. J. Garlick, A. F. Gibson, *Proc. Phys. Soc.* **60**, 574–590 (1948).
41. A. Baumann *et al.*, *J. Phys. Chem. Lett.* **6**, 2350–2354 (2015).
42. X. Liu *et al.*, *J. Mater. Chem. A Mater. Energy Sustain.* **4**, 17939–17945 (2016).
43. G. Niu, W. Li, J. Li, X. Liang, L. Wang, *RSC Advances* **7**, 17473–17479 (2017).
44. C. Wang *et al.*, *Sustain. Energy Fuels* **2**, 2435–2441 (2018).
45. N. J. Jeon *et al.*, *Nat. Energy* **3**, 682–689 (2018).
46. T.-Y. Yang *et al.*, *Adv. Sci.* **6**, 1900528 (2019).

ACKNOWLEDGMENTS

Funding: This work was supported by the Basic Science Research Program (NRF-2018R1A2A3074921), the Climate Change Program (NRF2015M1A2A2056542), and the Global Frontier Program (2012M3A6A7054861) through the National Research Foundation of Korea (NRF) funded by the Ministry of Science, ICT & Future Planning (MSIP). This work was also supported by the Defense Challengeable Future Technology Program of the Agency for Defense Development, Republic of Korea, and by a brand project (1.200030.01) of UNIST. Finally we thank the beamline staff at Pohang Accelerator Laboratory for supporting GIWAXS measurement. **Author contributions:** S.I.S. designed and supervised the research. G.K. and H.M. fabricated and characterized the perovskite films and devices. K.S.L. measured TSC. D.Y.L. conducted PL and TCSPC measurement. S.M.Y. measured UV-vis absorption. G.K. performed the stability tests of perovskite devices. S.I.S., H.M., and G.K. wrote the draft of the manuscript, and all authors contributed to writing the paper. **Competing interests:** G.K., H.M., and S.I.S. are inventors on a patent application (KR 10-2020-0074349) submitted by the Ulsan National Institute of Science and Technology that covers the $MDACl_2$ and Cs costabilized a-$FAPbI_3$. **Data and materials availability:** All data needed to evaluate the conclusions in the paper are present in the paper or the supplementary materials.

SUPPLEMENTARY MATERIALS

science.sciencemag.org/content/370/6512/108/suppl/DC1
Materials and Methods
Figs. S1 to S13
Table S1

24 April 2020; accepted 10 August 2020
10.1126/science.abc4417

Science

Impact of strain relaxation on performance of α-formamidinium lead iodide perovskite solar cells

Gwisu Kim, Hanul Min, Kyoung Su Lee, Do Yoon Lee, So Me Yoon and Sang Il Seok

Science **370** (6512), 108-112.
DOI: 10.1126/science.abc4417

Relieving unwanted strain

Although the α-phase of formamidinium lead iodide ($FAPbI_3$) has a suitable bandgap for use in solar cells, it must be stabilized with additional cations. These compositions can adversely affect the bandgap and produce lattice strain that creates trap sites for charge carriers. Kim *et al.* found that substituting small, equimolar amounts of cesium and methylenediammonium cations for formamidinium reduced the lattice strain and trap densities. The enhancement in open-circuit voltage led to a certified power conversion efficiency of 24.4%, and encapsulated devices retained 90% of their initial efficiency after 400 hours of maximal power point operating conditions.

Science, this issue p. 108